

See discussions, stats, and author profiles for this publication at: <https://www.researchgate.net/publication/308862095>

An accurate force regulation mechanism for handling fragile objects using pneumatic grippers

Conference Paper · July 2016

DOI: 10.1109/AIM.2016.7576798

CITATION

1

READS

72

2 authors, including:



Chao-Chieh Lan

National Cheng Kung University

79 PUBLICATIONS 1,645 CITATIONS

SEE PROFILE

An Accurate Force Regulation Mechanism for High-Speed Handling of Fragile Objects Using Pneumatic Grippers

Chih-Chieh Chen and Chao-Chieh Lan[✉], *Senior Member, IEEE*

Abstract—Controlling the gripping force on fragile objects has been a challenging task for industrial grippers. The solution often requires an electric gripper with embedded force sensors and control feedback. This approach is costly and leads to extra gripper complexity. To avoid damage while handling fragile objects, this paper presents a novel force regulation mechanism (FRM) to be installed on pneumatic grippers. Without using additional sensors and control, the FRM can passively produce an adjustable contact force between the gripper jaws and objects of various sizes. Together with pneumatic grippers that have a higher gripping speed, lower cost, and simpler structure, this approach offers a more attractive solution than the use of electric grippers. In this paper, the design and analysis of the FRM are presented. A prototype of the FRM is illustrated to demonstrate the effectiveness and accuracy of force regulation. This novel mechanism is expected to serve as a reliable alternative for fragile object manipulation.

Note to Practitioners—Pneumatic grippers are popular due to their low cost and simple structure. However, it is difficult to control the gripping force to handle fragile objects without damage. The FRM has a small size and can be easily installed on pneumatic grippers to provide fast force regulation. The gripping force depends on axial preload of the FRM rather than air pressure of the gripper. Axial preload is passively regulated using a screw or spacer. No additional source of power or sensor is required. The FRM has a large force adjustment range and can grip objects of various sizes using the same force. Applications include the automation in electronics, food, agricultural, and medical industries.

Index Terms—Compliant mechanism, constant force, force control, pick and place, pneumatic gripper, zero stiffness.

I. INTRODUCTION

A MECHANICAL gripper is a device with two or more jaws to pick and place an object. The jaws are symmetrically placed and rely on a particular actuation mechanism to transmit the input displacement to output linear or rotary gripping motion. Industrial grippers have jaws of high rigidity and wide gripping range so that they can handle heavy

and large objects. Dexterous grippers with multidegrees-of-freedom jaws or multiple jaws [1]–[4] have been developed to handle objects of different shapes. To process small and fragile objects, compliant grippers (e.g., [5]–[10]) have been developed. Compliant grippers are attractive in microscale manipulation because they can be monolithically fabricated. Various principles have been used for the actuation and sensing of compliant grippers.

Regardless of mechanism type, grippers can be electrically or pneumatically actuated. They are increasingly being used to handle fragile objects whose contact force cannot be too large, e.g., small plastic parts, fruits, vegetables, or living objects. In terms of gripping force, electric grippers are more preferable because their jaw closing position and speed can be continuously controlled by electric motors to match with objects of different sizes. To maintain safe handling of fragile objects, the contact surfaces on the jaws can be attached with force sensors based on piezoresistive [11], resistive [12], or capacitive principles. By using closed-loop force control, the gripping force can be controlled at a specific value that would not damage the objects. To ensure precise and stable force control, the gripping speed needs to be slow enough. This would require more cycle time for manipulation. In addition, external force sensors are usually expensive and may not be reliable in harsh industrial environments under repeated use.

In contrast to electric grippers, pneumatic grippers of the same sizes have simpler structures and larger gripping force. Their gripping speed is at least ten times faster than that of electric grippers. Given comparable specifications, they are one or even two orders-of-magnitude cheaper than electric grippers. Hence, pneumatic grippers are more popular in automation industry. However, the jaws of pneumatic grippers can only be controlled at fully open or closed position. Hence, it is impossible to control the gripping force using force sensors. Controlling the gripping force via air pressure regulation is possible. But the internal friction of a gripper and pressure drop along the pipeline would significantly limit the accuracy of gripping force control, especially if small gripping force is required. Hence, it is difficult to use pneumatic grippers to safely handle fragile objects.

It is also possible to use suction grippers [13] or grippers with compliant jaws [14], [15] to reduce the contact force on fragile objects. Suction grippers can eliminate the gripping force but are only suitable for objects with size larger than the

Manuscript received November 20, 2016; revised March 30, 2017 and June 2, 2017; accepted September 25, 2017. This paper was recommended for publication by Associate Editor C. C. L. Wang and Editor Y. Sun upon evaluation of the reviewers' comments. (Corresponding author: Chao-Chieh Lan.)

The authors are with the Department of Mechanical Engineering, National Cheng Kung University, Tainan, Taiwan (e-mail: cclan@mail.ncku.edu.tw).

Color versions of one or more of the figures in this paper are available online at <http://ieeexplore.ieee.org>.

Digital Object Identifier 10.1109/TASE.2017.2757527

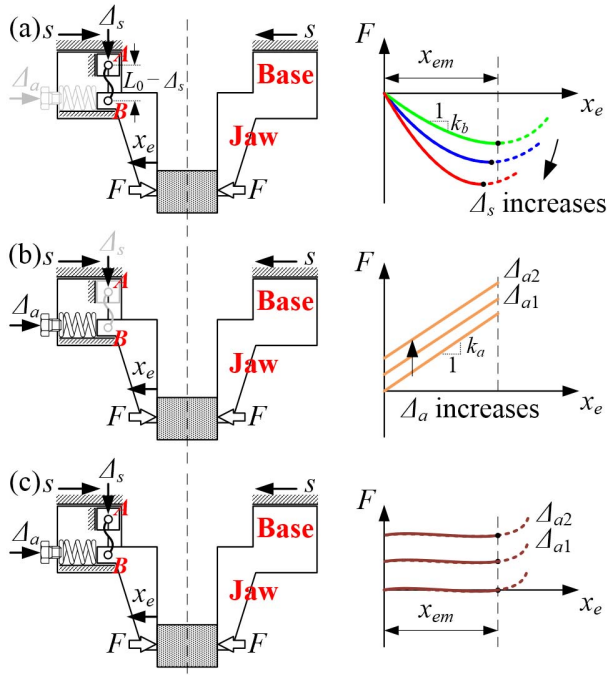


Fig. 1. F - x_e curves of a gripper with the FRM. (a) Lateral spring only. (b) Axial spring only. (c) Both lateral and axial springs.

suction cups. Compliant jaw grippers can reduce the gripping force on the object and at the same time conform to the object shape. But the gripping force cannot be controlled to meet the requirement of different force-sensitive objects. Due to compliance of the jaws, the position of the object relative to the jaws is uncertain after been picked. This will reduce the accuracy of placing an object from one place to another.

This paper aims to develop an accurate force regulation mechanism (FRM) for pneumatic grippers so that they can be readily used to provide high-speed manipulation of fragile objects without causing damage. This FRM can provide an adjustable constant gripping force that is independent of air pressure and object size. Constant-force mechanisms have been developed to deal with mating uncertainty [16] and vibration isolation [17]. Their merits in gripping mechanisms remain under-explored [18], [19]. The FRM is passive and has high reliability. The constant gripping force can be further adjusted by providing different axial preloads. In what follows, the design concept of the FRM is presented in Section II. This is followed by an analytical model in Section III to determine the optimal design parameters. A prototype of the FRM on a pneumatic gripper is illustrated in Section IV with simulation to show the constant force and force regulation ability. Static experiments in Section V and dynamic experiments in Section VI demonstrate the function of the FRM and actual performance of a pneumatic gripper with the FRM.

II. DESIGN CONCEPT

Fig. 1 shows a force-fit gripper with a pair of parallel rigid jaws. The FRM, which is illustrated on the left jaw, consists of a lateral spring and an axial spring. The lateral spring with stiffness k_s is placed along the vertical direction. Its two

ends are pin connected at point A of the vertical slider and point B of the left jaw. The lateral spring has an undeformed length of L_0 and preload Δ_s . Thus, the distance between A and B is $L_0 - \Delta_s$. The axial spring with stiffness k_a is placed along the horizontal direction. It is given an adjustable preload Δ_a through, for example, an adjustment screw. At the equilibrium position, points A and B are aligned vertically. When the base of the gripper is given a displacement s by a pneumatic cylinder to contact a small rigid object, a relative displacement x_e between the jaw and base is generated. The jaws will produce a gripping force F . The operational range of the jaw is denoted as x_{em} .

Fig. 1(a) shows the F - x_e curve when considering only the lateral spring. Depending on the amount of preload Δ_s , the curve will exhibit different magnitudes of negative stiffness, and then turn to positive stiffness. The dot represents the position of zero stiffness. Equation (1a) shows the expression of the F - x_e curve. The stiffness of the F - x_e curve is denoted as k_b and can be obtained by differentiating the F - x_e curve with respect to x_e , as shown in (1b)

$$F = k_s x_e \left\{ 1 - \frac{1}{[(L_0 - \Delta_s)^2 + x_e^2]^{1/2}} \right\} \quad (1a)$$

$$k_b = k_s \left\{ 1 - \frac{L_0(L_0 - \Delta_s)^2}{[(L_0 - \Delta_s)^2 + x_e^2]^{3/2}} \right\}. \quad (1b)$$

For each curve in Fig. 1(a), the solid-line segment before the dot is nearly straight. The stiffness at $x_e = 0$ can be used to represent the stiffness of the solid-line segment

$$k_b(x_e = 0) = k_s [1 - L_0/(L_0 - \Delta_s)]. \quad (2)$$

As can be observed in (2), the magnitude of negative stiffness increases with the increase of preload Δ_s .

Fig. 1(b) shows the F - x_e curve when considering only the axial spring. The curve exhibits positive stiffness. The preload Δ_a will shift the curve upward without changing the stiffness. The amount of upward shift increases with the increase of preload. When the lateral and axial springs are connected in parallel, their respective stiffness is added to generate the gripping stiffness k

$$k = k_a + k_b. \quad (3)$$

When the magnitude of k_b is adjusted to match with k_a , the gripping stiffness k will be nearly zero. Fig. 1(c) shows the combined F - x_e curve. Within the operational range x_{em} , the curve exhibits nearly constant gripping force (zero stiffness) despite some force variation. By changing the axial preload (e.g., from Δ_{a1} to Δ_{a2}), the magnitude of the gripping force can be adjusted. The gripping force variation within the operational range is related to the axial preload by

$$\text{Force variation} = F - k_a \Delta_a. \quad (4)$$

By attaching the FRM to one or both of the jaws, the gripping force can easily be controlled at a prespecified value. While the FRM is applicable to both pneumatic and electric grippers, its benefits on pneumatic grippers are more significant. Fig. 2(a) shows a schematic of a pneumatic gripper without the FRMs. The jaw base has a stroke of s_j and opening of R_x . When actuated, the jaws will push against the object with a displacement of s . For an object size of R ,

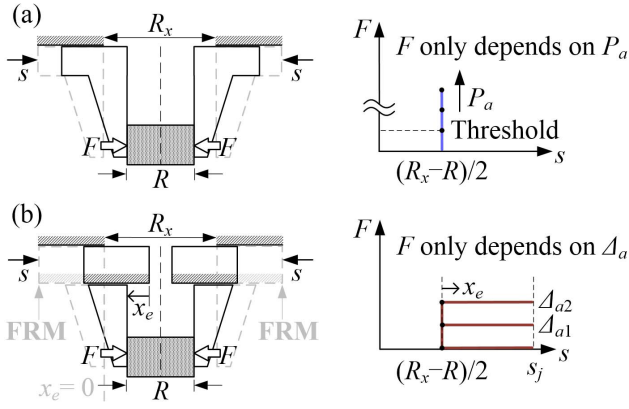


Fig. 2. (a) Controlling gripping force using air pressure regulation. (b) Controlling gripping force using the FRM.

the displacement of each jaw is $(R_x - R)/2$. The gripping force depends on the air pressure P_a , which is difficult to control. To overcome the internal friction force, the air pressure of pneumatic grippers needs to exceed a certain threshold (e.g., 0.2 MPa) in order to fully actuate the jaws. Since the friction force varies, a very high air pressure is usually used (e.g., 0.5 or 0.6 MPa) to ensure successful gripping over repeated cycles. Hence, the gripping force is very large.

Fig. 2(b) shows another pneumatic gripper with two FRMs attached to the bases. Both FRMs are adjusted to have a specific preload Δ_a . When actuated, the gripper base will complete the full stroke s_j . Each jaw will have a relative displacement x_e with respect to the gripper base. As long as the value of x_e is less than x_{em} , the gripping force will be maintained at the prescribed force level. To achieve this, the size of the object, jaw opening, and jaw stroke should satisfy the following inequality:

$$R_x - 2s_j \leq R \leq R_x - 2s_j + 2x_{em}. \quad (5)$$

As (5) indicates, the object size has a variation of $2x_{em}$ while the gripping force is independent of the size variation. The gripping force is also independent of the air pressure. Thus, large air pressure can be used to ensure proper closing of the jaws while the gripping force can be maintained at a specific low value. Unlike grippers that use compliant jaws to regulate the gripping force, the FRM can still utilize rigid jaws while the gripping force can accurately be regulated. This is advantageous because the position of the object is more predictable.

Using the FRM, adjustable force regulation is now possible for pneumatic grippers. The FRM is passive and requires no active force control scheme. This avoids the use of electric grippers with embedded force sensors, which are much more costlier than pneumatic grippers. Since pneumatic grippers are used, force regulation speed is higher than electric grippers with force control.

III. ANALYTICAL DESIGN MODEL

For a given axial preload of the FRM, the force variation within the operational range has to be small enough in order to

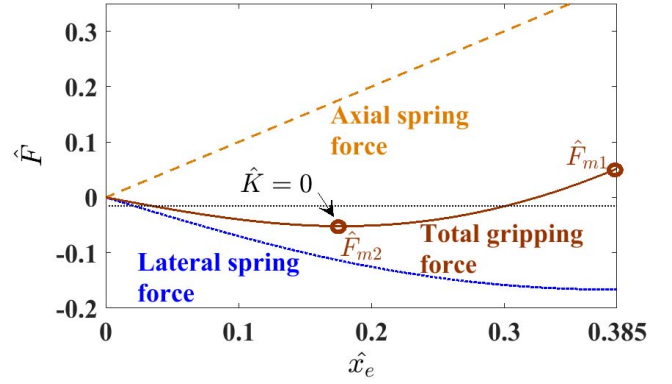


Fig. 3. Dimensionless force-to-displacement curves.

provide precise output force regulation. An analytical design model is presented in this section to determine the optimal values of the lateral spring stiffness and lateral spring preload such that the force variation is minimized.

The gripping force F is the sum of the force from the axial and lateral springs. Integrating (3) with respect to x_e , the gripping force can be written as follows:

$$F = k_a(x_e + \Delta_a) + k_s x_e \{1 - L_0 / [(L_0 - \Delta_s)^2 + x_e^2]^{1/2}\}. \quad (6)$$

The first and second terms on the right side of (6) represent the contribution from axial and lateral springs, respectively. For clarity of analysis, the jaw displacement, lateral preload, and gripping force are nondimensionalized as

$$\hat{x}_e = x_e / L_0; \quad \hat{\Delta}_s = \Delta_s / L_0; \quad \hat{F} = (F - k_a \Delta_a) / k_a L_0. \quad (7)$$

Using (7), (6) can be nondimensionalized as

$$\hat{F} = \hat{x}_e \{1 + \alpha [1 - ((1 - \hat{\Delta}_s)^2 + \hat{x}_e^2)^{-1/2}]\} \quad (8)$$

where $\alpha = k_s / k_a$ denotes the stiffness ratio of the axial and lateral springs. The value of \hat{F} is ideally zero for no force variation and can be used to indicate the force variation for a set of given α and $\hat{\Delta}_s$. We define \hat{F}_m , the maximum absolute value of \hat{F} in the operational range, as the force variation of an $\hat{F} - \hat{x}_e$ curve. The nondimensional gripping stiffness \hat{K} can be obtained based on (3)

$$\hat{K} = 1 + \alpha \{1 - (1 - \hat{\Delta}_s)^2 / [(1 - \hat{\Delta}_s)^2 + \hat{x}_e^2]^{3/2}\}. \quad (9)$$

Setting (9) equal to zero, we obtain the gripping position \hat{x}_e that produces zero gripping stiffness

$$\hat{x}_e = \{(1 - \hat{\Delta}_s)^{4/3} [\alpha / (\alpha + 1)]^{2/3} - (1 - \hat{\Delta}_s)^2\}^{1/2}. \quad (10)$$

As an illustration, Fig. 3 shows the $\hat{F} - \hat{x}_e$ curves for $\alpha = 1.729$ and $\hat{\Delta}_s = 0.456$. From (10), the gripping stiffness \hat{K} is zero when $\hat{x}_e = 0.176$. As \hat{x}_e increases, the stiffness magnitude of the lateral spring curve reduces to zero. Further increase in \hat{x}_e would make the stiffness positive and cannot be used to counteract the positive stiffness of the axial spring. To avoid excessive force variation, the position where the lateral spring curve has zero stiffness should be considered as the limit of \hat{x}_e . This position can be obtained by setting the second term in (9)

equal to zero. Thus, the operational range of \hat{x}_e , which is defined as \hat{x}_{em} , should be less than this limit

$$\hat{x}_{em} \leq [(1 - \hat{\Delta}_s)^{4/3} - (1 - \hat{\Delta}_s)^2]^{1/2}. \quad (11)$$

According to (11), the maximum value of \hat{x}_{em} should be 0.385 when $\hat{\Delta}_s = 0.456$. The maximum value of \hat{F} may occur within the operational range or at the endpoint where $\hat{x}_e = \hat{x}_{em}$, depending on the value of α . At $\hat{x}_e = \hat{x}_{em}$, the nondimensional \hat{F} is denoted as \hat{F}_{m1} , as shown in Fig. 3. The expression of \hat{F}_{m1} can be obtained by replacing \hat{x}_e in (8) by \hat{x}_{em}

$$\hat{F}_{m1} = \hat{x}_{em} \{1 + \alpha [1 - ((1 - \hat{\Delta}_s)^2 + \hat{x}_{em}^2)^{-1/2}]\}. \quad (12)$$

As shown in Fig. 3, we denote the maximum magnitude of \hat{F} within the operational range as \hat{F}_{m2} . The value of \hat{F}_{m2} can be obtained by substituting (10) into (8)

$$\begin{aligned} \hat{F}_{m2} = & \alpha \{1 - (1 - \hat{\Delta}_s)^{2/3} [\alpha / (\alpha + 1)]^{-2/3}\}^{1/2} \\ & - (1 + \alpha) \{ (1 - \hat{\Delta}_s)^{4/3} [\alpha / (\alpha + 1)]^{2/3} - (1 - \hat{\Delta}_s)^2 \}^{1/2}. \end{aligned} \quad (13)$$

Variables \hat{F}_{m1} and \hat{F}_{m2} in (12) and (13) are both functions of $\hat{\Delta}_s$ and α . The force variation \hat{F}_m is the maximum of the two. For a given $\hat{\Delta}_s$, \hat{F}_{m1} decreases and \hat{F}_{m2} increases as α increases. There will be a value of α such that \hat{F}_{m1} and \hat{F}_{m2} are equal. At this α , the force variation \hat{F}_m is minimum. Equating \hat{F}_{m1} in (12) and \hat{F}_{m2} in (13), we can obtain a function f_1 that depends on \hat{x}_{em} , $\hat{\Delta}_s$, and \hat{F}_m

$$f_1(\hat{x}_{em}, \hat{\Delta}_s, \hat{F}_m) = 0. \quad (14)$$

Equation (14) can be used to solve for \hat{F}_m for a specific set of $\hat{\Delta}_s$ and \hat{x}_{em} . Once \hat{F}_m is determined, the value of α can be obtained using the rearrangement of (8)

$$\alpha = (1 - \hat{F}_m / \hat{x}_{em}) \{1 / [(1 - \hat{\Delta}_s)^2 + \hat{x}_{em}^2]^{1/2} - 1\}^{-1}. \quad (15)$$

Since this value of α offers the minimum variation of \hat{F} , it should be chosen for each value of $\hat{\Delta}_s$. Because the $F-x_e$ curve in Fig. 1(a) also depends on the value of $\hat{\Delta}_s$, the optimal $\hat{\Delta}_s$ that produces the smallest \hat{F}_m further needs to be determined. To do so, we differentiate (14) with respect to $\hat{\Delta}_s$ and set $d\hat{F}_m/d\hat{\Delta}_s$ equal to zero to obtain the following:

$$f_2(\hat{x}_{em}, \hat{\Delta}_s, \hat{F}_m) = 0. \quad (16)$$

Thus, (14) and (16) can be simultaneously solved to determine the values of $\hat{\Delta}_s$ and \hat{F}_m for a given \hat{x}_{em} . Once $\hat{\Delta}_s$ is obtained, the value of α can be determined using (15). The combination of $\hat{\Delta}_s$ and α makes the force variation minimal.

To show the effects of α and $\hat{\Delta}_s$ on the $\hat{F}-\hat{x}_e$ curve, we consider the case where $\hat{x}_{em} = 0.3$. According to (14)–(16), the optimal values of α and $\hat{\Delta}_s$ would be 2.073 and 0.376, respectively. The value of \hat{F}_m is 0.024. To compare the effects of α and $\hat{\Delta}_s$, their optimal values are multiplied or divided by 1.5. The corresponding force variations are listed in Table I. As can be seen, the value of \hat{F}_m is both sensitive to $\hat{\Delta}_s$ and α . When $\hat{\Delta}_s$ is fixed and α varies from its optimal value, the force variation increases significantly. When α is fixed and $\hat{\Delta}_s$ varies, the increase of force variation is larger. Similar effects can be expected for other values

TABLE I
EFFECTS OF α AND $\hat{\Delta}_s$ ON \hat{F}_m ($\hat{x}_{em} = 0.3$)

$\hat{\Delta}_s = 0.376$		$\alpha = 2.073$	
$\alpha = 2.073 \div 1.5$	$\hat{F}_m = 0.116$	$\hat{\Delta}_s = 0.376 \div 1.5$	$\hat{F}_m = 0.151$
$\alpha = 2.073$	$\hat{F}_m = 0.024$	$\hat{\Delta}_s = 0.376$	$\hat{F}_m = 0.024$
$\alpha = 2.073 \times 1.5$	$\hat{F}_m = 0.130$	$\hat{\Delta}_s = 0.376 \times 1.5$	$\hat{F}_m = 0.263$

TABLE II
GIVEN PARAMETERS OF THE FRM

Operational range, x_{em}	5 mm
Lateral spring length, L_0	16.67 mm
Axial spring stiffness, k_a	1.62 N/mm
Force adjustability	0~10 N

TABLE III
CALCULATED PARAMETERS OF THE FRM

Axial spring preload, Δ_a	0~6.173 mm
Lateral spring preload, Δ_s	6.267 mm
Force variation, F_m	0.639 N
Stiffness ratio, α	2.073
Lateral spring stiffness, k_s	3.359 N/mm

of \hat{x}_{em} . The force variation decreases with the decrease of \hat{x}_{em} . Equations (14)–(16) should be used for the FRM to obtain a nearly constant gripping force curve for a given \hat{x}_{em} .

IV. REALIZATION OF THE FORCE REGULATION MECHANISM

A. Parameter Design of the Force Regulation Mechanism

The analytical model presented in Section III can be used to determine the parameters of an FRM of various sizes and force magnitudes. As an illustration, we consider a set of given parameters listed in Table II. The operational range x_{em} and lateral spring length L_0 are chosen to fit in a small-size pneumatic gripper. The corresponding value of \hat{x}_{em} would be 0.3. Stiffness of $k_a = 1.62$ N/mm is used for the axial spring. Since most electric or pneumatic grippers do not provide force less than 10 N, we specify the force adjustability to be 0~10 N in order to handle objects that are sensitive to gripping force in this range.

Based on the given parameters in Table II, the other parameters of the FRM can be calculated, as listed in Table III. To achieve the force range of 10 N, the deformation of the axial spring would be 6.173 mm. The rest of the parameters are calculated using (14)–(16). Specifically, the lateral spring preload Δ_s and force fluctuation F_m can be obtained from (14) and (16). The corresponding force fluctuation is 0.64 N. The force fluctuation is nearly 6% of the maximum force 10 N. This amount can be considered small for many applications. The optimal stiffness $\alpha = 2.07$ is obtained using (15). This determines the lateral spring stiffness k_s , which is equal to 3.359 N/mm. The values of α and Δ_s can assure a minimum force fluctuation. To make the force fluctuation even smaller, we need to choose a smaller x_{em} or larger L_0 .

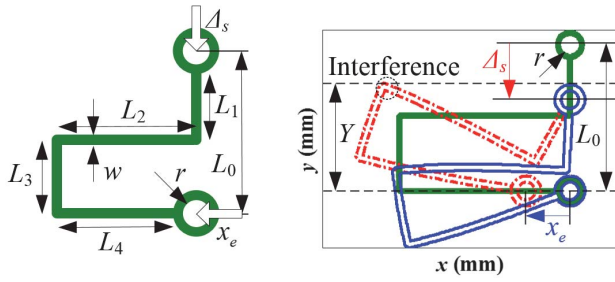


Fig. 4. (a) Schematic of planar spring design. (b) Deformation after preload and gripping.

B. Design of the Lateral Spring

As shown in Fig. 1, the lateral spring needs to be pin connected at the two ends. The lateral spring will rotate during its compression. Typical compression coil springs do not have pinned ends and are vulnerable to buckling if the deformation is not properly constrained. Hence, a coil spring cannot be easily used as the lateral spring without compromising size and complexity. To minimize the lateral spring size to meet stringent space requirement, we propose a design of using a planar spring to serve as the lateral spring. Fig. 4(a) shows the schematic of the planar spring design. Unlike coil springs, the planar spring is a 2-D structure. As an illustration, the planar spring consists of straight beam segments connected at right angles. The beam segments have a constant in-plane thickness. The O-shaped rings at the ends are for mounting pins to rotate with respect to the connecting parts. The out-of-plane thickness t , in-plane thickness w , and length of each segment (L_1 – L_4) determine the stiffness k_s . Fig. 4(b) shows an illustrative spring deformed shape when both Δ_s and x_e are present. As can be seen, the shape of the planar spring is chosen such that it does not exceed the interference line when deformed. The interference line prevents the rotated planar spring from contacting the base of the pneumatic gripper.

An optimization has been formulated in (17) to find the dimensions of the beam segments to meet the stiffness requirement while interference is avoided. To ensure sufficient reliability, the maximum spring stress σ_m during deformation should be minimized

$$\begin{aligned} & \text{Minimize } \sigma_m \\ & \text{s.t. } \begin{cases} g_1 : L_0 = L_1 + L_3; & g_2 : L_2 = L_4 + r + w \\ g_3 : Y \leq L_0 + r + w - \Delta_s; & g_4 : k_s = 3.359 \text{ N/mm.} \end{cases} \end{aligned} \quad (17)$$

In (17), g_1 – g_2 are the length constraints. Constraint g_3 is used to ensure that the spring shape remains within a prescribed height Y in order to not interfere with its neighboring parts. Table IV lists the given and optimized parameters. We use plastic mold steel (S-STAR) as the material of the planar spring. The optimization is carried out using *fmincon()* in MATLAB while the generalized multiple shooting method (GMSM) [20] is used for the larger deformation analysis of the planar spring. The dimension of the optimized planar spring is $21.6 \times 20.1 \times 2 \text{ mm}^3$. The maximum stress is 1.12 GPa at $\Delta_s = 6.267 \text{ mm}$ and $x_e = 0 \text{ mm}$.

TABLE IV
GIVEN AND OPTIMIZED PARAMETERS OF THE PLANAR SPRING

Given	Young's modulus (S-STAR) $E = 215.5 \text{ GPa}$
	Yield stress (S-STAR) $\sigma_y = 1.54 \text{ GPa}$
	Out-of-plane thickness $t = 4 \text{ mm}$
	O-shaped ring radius $r = 1 \text{ mm}$
Optimized	In-plane thickness $w = 0.727 \text{ mm}$
	$L_1 = 6.358 \text{ mm}$, $L_2 = 19.502 \text{ mm}$, $L_3 = 8.582 \text{ mm}$, $L_4 = 17.775 \text{ mm}$
	Maximum stress $\sigma_m = 1.12 \text{ GPa}$

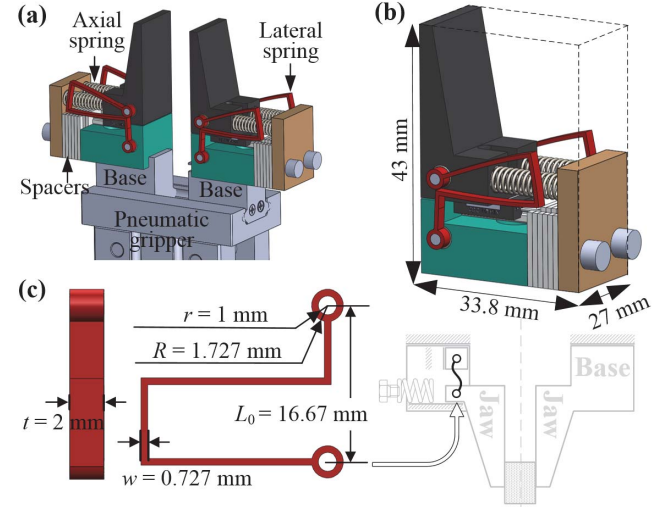


Fig. 5. (a) Gripper prototype with two FRMs. (b) Dimension of the FRM. (c) Dimension of the lateral spring.

The planar spring is not limited to the shape illustrated in Fig. 4. More complicated shapes can be used as long as the planar spring can produce the desired stiffness without causing interference.

C. Force Regulation Mechanism Prototype

The FRM needs to have a small size in order to be mounted on various types of jaws without interfering with other components. To minimize the FRM size, we propose a prototype of two FRMs installed on a commercially available pneumatic gripper. The pneumatic gripper has a stroke s_j of 5.4 mm and opening R_x of 12.6 mm. As shown in Fig. 5(a) and (b), the dimension of each FRM is $43 \times 33.8 \times 27 \text{ mm}^3$. The FRMs are designed based on the parameters listed in Tables II and IV. Two compression coil springs with stiffness of 0.81 N/mm and natural length of 21.5 mm are placed inside the FRM to serve as the axial spring. Hence, the equivalent value of k_a is 1.62 N/mm. The coil springs can easily be preloaded by changing the number of spacers. Each spacer has a thickness of 1.15 mm, and thus can increase or decrease the gripping force by 1.69 N. A precision screw may also be used to provide continuous adjustment. Linear actuators are possible if automatic adjustment is required. Fig. 5(c) shows the dimension of the lateral spring. To maintain symmetry, two identical planar springs are placed on the two sides of each FRM. To match

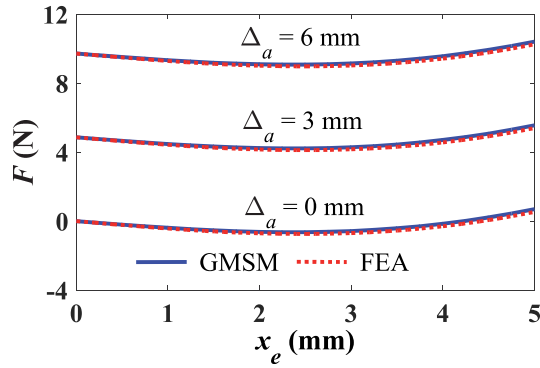
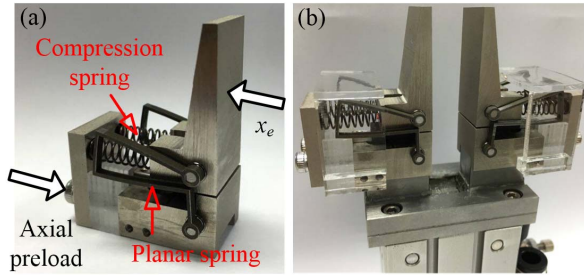
Fig. 6. F - x_e curves of the FRM.

Fig. 7. (a) Close view of the FRM. (b) Actual pneumatic gripper with an FRM on each jaw.

with the stiffness requirement of 3.359 N/mm, the planar spring on each side has an out-of-plane thickness of 2 mm while other dimensions are the same as those in Table IV.

D. Finite-Element Analysis and Verification

This section presents a finite-element analysis (FEA) to verify the results obtained in Sections IV-A and IV-B. The CAD model in Fig. 5 is imported into ANSYS to perform the static analysis. All the joints are assumed frictionless. Fig. 6 shows the combined F - x_e curves when considering both the axial and lateral springs. Solid and dotted curves are computed using the GSM and FEA, respectively. The computed force variation is 0.639 N for the GSM curve, which is consistent with the analytical F_m value in Table III. The average gripping forces are -0.27 , 4.59 , and 9.45 N for $\Delta_a = 0$, 3 , and 6 mm, respectively. For all the three preloads, the FEA and GSM results nearly match. The fluctuation of the FEA curves is slightly smaller than that of the GSM curves.

For $\Delta_a = 0$ – 6 mm, the range of force adjustment is 0 – 9.72 N. This range depends on the achievable axial preload and is independent of the lateral spring deformation. If larger gripping force is required, the axial preload should be increased. For example, a 12-mm preload can provide a force adjustment from 0 to nearly 20 N.

V. STATIC EXPERIMENT VERIFICATIONS

Based on the CAD model in Fig. 5, a FRM has been fabricated, assembled, and attached to a pneumatic gripper. Fig. 7(a) shows a close view of the FRM, and Fig. 7(b) shows a pneumatic gripper with a FRM on each jaw. The axial springs were commercially available while the two planar springs

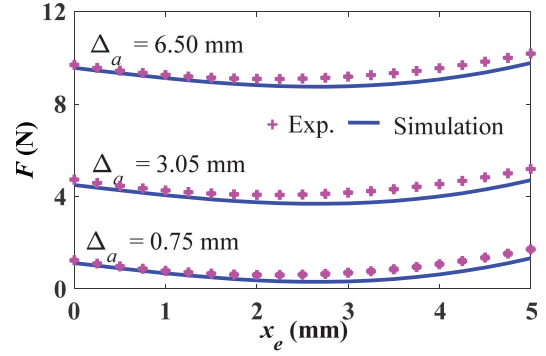
Fig. 8. Experimental F - x_e curves.

TABLE V
COMPARISONS OF STATIC GRIPPING FORCE USING
DIFFERENT PRELOADS (N)

Δ_a (mm)	Calculated average of F	Experimental average of F	Experimental F_m
0.75	0.633	0.913	0.637
3.05	4.018	4.395	0.663
6.50	9.096	9.411	0.609

were fabricated using wire electrical-discharge machining. The measured k_s and k_a were 3.22 and 1.47 N/mm, respectively. Due to manufacturing imperfections, these stiffness values are slightly smaller than the desired ones in Tables II and III. The corresponding values of α and F_m are 2.19 and 0.82 N, respectively. The gripping force adjustment was made using different number of spacers where each spacer has a thickness of 1.15 mm. When there are five, three, and no spacers, the axial preloads are 0.75, 3.05, and 6.50 mm, respectively. The total weight of the FRM was 57 g.

An experiment has been conducted to measure the actual F - x_e curves of the FRM. A linear actuator drove the FRM and jaw to contact two stationary load cells (FUTEK LSB 200, 0.1% accuracy) at a slow speed (0.5 mm/s). The load cells measured the gripping force. Different preload adjustments were tested: $\Delta_a = 0.75$, 3.05 , and 6.50 mm. Each preload was repeated three times to obtain the average F - x_e curve. Fig. 8 shows the average F - x_e curves for x_e from 0 to 5 mm. The three curves show relatively constant gripping force. The average gripping forces are 0.913, 4.395, and 9.411 N for $\Delta_a = 0.75$, 3.05 , and 6.50 mm, respectively. The corresponding simulation curves (obtained using the GSM) are also compared in Fig. 8. The average force values for the simulation curves are 0.633, 4.018, and 9.096 N for $\Delta_a = 0.75$, 3.05 , and 6.50 mm, respectively. Table V lists the numerical values. As shown in Fig. 8, the simulated F - x_e curves are almost the same as the experimental counterparts. The difference increases with the increase of x_e . The difference pattern is almost the same for all the three cases. This difference is mainly due to imperfect assembly of the FRM such that the friction force increases with the increase of x_e .

VI. DYNAMIC EXPERIMENT VERIFICATIONS

A. Effect of Object Compliance

The experiment in Section V verified the static F - x_e curves. In practice, the gripper is actuated by air cylinders, and the

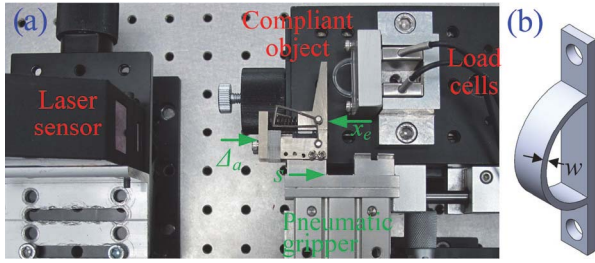


Fig. 9. (a) Experimental setup to measure the dynamic gripping force. (b) Compliant object with thickness w .

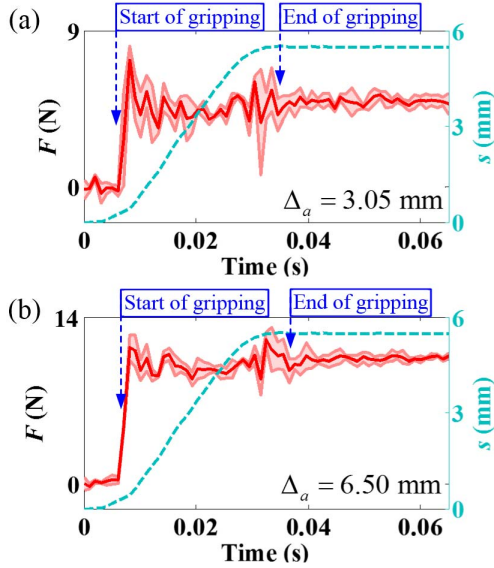


Fig. 10. Experimental gripping force versus time for different preloads. (a) $\Delta_a = 3.05$ mm. (b) $\Delta_a = 6.50$ mm.

dynamics during the gripping motion may affect the force response. Two experiments are given in this section to study the effect of dynamics on the gripping force. Fig. 9(a) shows the setup of the first experiment. The jaw and FRM on the left side of the gripper were pneumatically actuated, rather than by a linear actuator. A semicircular compliant object made of acrylic with a radius of 8.5 mm was attached to a set of two load cells for contact force measurement. Fig. 9(b) shows the compliant object. One object has in-plane thickness w of 1 mm and the other of 1.5 mm. The displacement s of the base was obtained using a laser displacement sensor. This experiment was to verify the FRM of different axial preloads for gripping objects of different stiffnesses. Fig. 10(a) and (b) shows the gripping force versus time of $\Delta_a = 3.05$ and 6.50 mm, respectively. The object with $w = 1$ mm was used and air pressure was 0.5 MPa. Each preload was repeated three times to obtain the error band. The start and end of gripping are indicated in Fig. 10(a) and (b). The gripping time was about 0.03 s. The displacement s of the base was also plotted in Fig. 10(a) and (b). The transient force variation when s increases from 0 to 5.4 mm was due to the inertial force of the jaw. After the end of gripping ($t > 0.04$ s), the gripping force became stable.

Table VI lists the experimental average gripping force after $t = 0.04$ s. Both the results of $w = 1$ and 1.5 mm

TABLE VI
COMPARISON OF GRIPPING FORCE USING DIFFERENT
OBJECT COMPLIANCES (N)

	$\Delta_a = 3.05$ mm	$\Delta_a = 6.50$ mm
Thickness = 1 mm	4.59	9.53
Thickness = 1.5 mm	4.74	10.00
Simulation	4.61	9.68

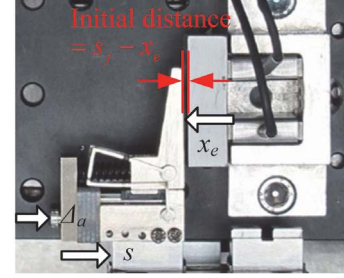


Fig. 11. Experimental setup to study the effects of jaw displacement and air pressure.

are presented. The experimental gripping force matched well with those obtained by simulation. Due to the object deformation, an object with smaller stiffness would only result in a smaller displacement x_e of the jaw when compared with the same object of larger stiffness. As shown in Fig. 8, the gripping force F is nearly independent of the displacement x_e in the operational range. Hence, the jaw with the FRM can provide nearly the same gripping force for objects with a wide range of stiffnesses.

B. Effects of Jaw Displacement and Air Pressure

The second experiment shown in Fig. 11 is to study the effects of jaw displacement x_e and air pressure P_a on the gripping force. Different from that in Fig. 9(a), the compliant object was removed. The jaw directly contacted the rigid surface. The two load cells behind the rigid surface recorded the gripping force. The rigid surface allowed accurate measurement of the initial distance between the jaw and the contact surface. When gripping an object, the jaw displacement x_e depends on both the object size and object deformation. Since deformation is usually small, we consider only the effect of jaw displacement resulting from different object sizes. The relationship is expressed as follows:

$$\text{Initial distance} = (R_x - R)/2 = s_j - x_e. \quad (18)$$

Thus, different object sizes R can be emulated by changing the initial distance between the jaw and rigid surface. The corresponding jaw displacement x_e would also change.

Table VII lists the comparison of using different jaw displacements. Same as those in Table VI, the values in Table VII were the average gripping force after $t = 0.04$ s. The air pressure was 0.5 MPa. For both cases of $\Delta_a = 3.05$ and 6.50 mm, the simulation and experimental results matched well. For each case, the gripping force remained roughly the same for $x_e = 2.9 \sim 4.9$ mm despite some force variation.

TABLE VII
COMPARISON OF GRIPPING FORCE AT DIFFERENT
JAW DISPLACEMENTS (N)

x_e (mm)	Experiment at $\Delta_a = 3.05$ mm	Simulation at $\Delta_a = 3.05$ mm	Experiment at $\Delta_a = 6.50$ mm	Simulation at $\Delta_a = 6.50$ mm
4.9	4.75	4.61	9.64	9.68
3.9	3.72	3.94	9.05	9.02
2.9	3.53	3.68	8.85	8.76

TABLE VIII
COMPARISON OF GRIPPING FORCE AT DIFFERENT VALUES OF P_a (N)

P_a (MPa)	$\Delta_a = 0.75$ mm	$\Delta_a = 3.05$ mm	$\Delta_a = 6.50$ mm	Without the FRM
0.4	1.43	4.79	9.49	33
0.5	1.37	4.75	9.64	42
0.6	1.46	4.68	9.48	50
Simulation	1.22	4.61	9.68	-

Since the operational range of x_e is 5 mm, the FRM can handle objects with maximum size variation of 10 mm using nearly the same gripping force.

To study the effect of air pressure on the gripping force, three different air pressures were tested: $P_a = 0.4, 0.5$, and 0.6 MPa. For each P_a , preloads of $0.75, 3.05$, and 6.50 mm were used. Jaw displacement was 4.9 mm for all the tests. The gripping forces are listed in Table VIII. Higher air pressure results in higher actuation force of the base. But the closing velocities of the jaws are nearly the same at 200 mm/s. Hence, for each preload, the transient and steady-state gripping forces were nearly the same for the three different air pressures. The gripping force is shown to be independent of the air pressure and only depends on the axial preload. The results also agree well with simulation values listed in the last row of Table VIII. The maximum difference of the experimental values at a specific preload is nearly 0.2 N. Hence, 0.2 N can be viewed as the accuracy of the force adjustability for different pressures. This accuracy is comparable to many industrial force sensors.

As a comparison, the gripping forces without using the FRM are also listed in the last column of Table VIII. The gripping force is almost proportional to the air pressure. When a pressure of 0.6 MPa is used, the gripping force reaches 50 N, which is very large and would damage many fragile objects. The smallest force is 17 N when $P_a = 0.2$ MPa. Force below 17 N is not achievable because 0.2 MPa is nearly the threshold pressure to actuate the gripper. Thus, using the FRM can increase the force adjustability of pneumatic grippers.

As shown in Fig. 10, the time to achieve the desired gripping force is merely 0.03 s, which is independent of the preload, air pressure, and jaw displacement. If an electric gripper with force sensor were used to control the gripping force, it would be difficult to achieve the same time due to motor response and control stability limits. Hence, the FRM with pneumatic gripper can achieve accurate force regulation at a much higher speed. This can greatly reduce the cycle time of fragile object manipulation.

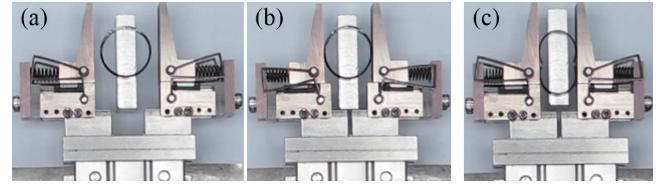


Fig. 12. Snapshots of gripping a circular ring. (a) Initial position. (b) Closed position with $\Delta_a = 3.05$ mm. (c) Closed position with $\Delta_a = 6.50$ mm.

C. Effect of Gripping Force on Fragile Objects

Fig. 12 shows three snapshots of gripping a circular ring. To clearly represent a fragile object, this circular ring was made of acrylic and had a diameter of 20 mm, in-plane thickness of 0.7 mm, and out-of-plane thickness of 4.8 mm. Fig. 12(a) shows the initial position when $s = 0$ mm while Fig. 12(b) and (c) shows the closed positions when $s = 5.4$ mm. Axial preloads of 3.05 and 6.50 mm were used for the gripping motion in Fig. 12(b) and (c), respectively. In Fig. 12(b), the ring can be firmly gripped by the FRM using a gripping force of 4.4 N. In Fig. 12(c), the excessive gripping force (9.4 N) damaged the ring. These two snapshots demonstrate the sensitivity of fragile objects to gripping force. The FRM can provide proper gripping force to handle these objects without causing damage.

VII. CONCLUSION

In this paper, we have presented the design, analysis, and experiment of an FRM to passively provide adjustable constant gripping force on fragile objects of various sizes. The overall mechanism is compact and can be readily installed on small pneumatic grippers for industrial manipulation. The static and dynamic experiments showed the accuracy of gripping force regulation at a high jaw speed. Based on the demonstrated prototype, the gripping force can easily be adjusted from 0 to 10 N while the object size variation is 10 mm. The prescribed gripping force was independent of the air pressure. The advantages over force controlled electric grippers or pneumatic grippers without the FRMs were clearly shown. We expect the FRM can provide a cost-effective industrial solution to safely handle fragile objects.

REFERENCES

- [1] A. Wolf, R. Steinmann, and H. Schunk, *Grippers in Motion: The Fascination of Automated Handling Tasks*. Springer, 2006.
- [2] F. Chen, F. Cannella, C. Canali, T. Hauptman, G. Sofia, and D. Caldwell, "In-hand precise twisting and positioning by a novel dexterous robotic gripper for industrial high-speed assembly," in *Proc. IEEE Int. Conf. Robot. Autom. (ICRA)*, May/Jun. 2014, pp. 270–275.
- [3] B. Kehoe, D. Warrier, S. Patil, and K. Goldberg, "Cloud-based grasp analysis and planning for tolerated parts using parallelized Monte Carlo sampling," *IEEE Trans. Autom. Sci. Eng.*, vol. 12, no. 2, pp. 455–470, Apr. 2015.
- [4] J. Su, H. Qiao, Z. Ou, and Z. Y. Liu, "Vision-based caging grasps of polyhedron-like workpieces with a binary industrial gripper," *IEEE Trans. Autom. Sci. Eng.*, vol. 12, no. 3, pp. 1033–1046, Jul. 2015.
- [5] C.-C. Lan, C.-M. Lin, and C.-H. Fan, "A self-sensing microgripper module with wide handling ranges," *IEEE/ASME Trans. Mechatronics*, vol. 16, no. 1, pp. 141–150, Feb. 2011.
- [6] A. N. Reddy, N. Maheshwari, D. K. Sahu, and G. K. Ananthasuresh, "Miniature compliant grippers with vision-based force sensing," *IEEE Trans. Robot.*, vol. 26, no. 5, pp. 867–877, Oct. 2010.

- [7] L. Wang, L. Ren, J. K. Mills, and W. L. Cleghorn, "Automated 3-D micrograsping tasks performed by vision-based control," *IEEE Trans. Autom. Sci. Eng.*, vol. 7, no. 3, pp. 417–426, Jul. 2010.
- [8] M. Rakotondrabe and I. A. Ivan, "Development and force/position control of a new hybrid thermo-piezoelectric microgripper dedicated to micromanipulation tasks," *IEEE Trans. Autom. Sci. Eng.*, vol. 8, no. 4, pp. 824–834, Oct. 2011.
- [9] Q. Xu, "Design and development of a novel compliant gripper with integrated position and grasping/interaction force sensing," *IEEE Trans. Autom. Sci. Eng.*, vol. 14, no. 3, pp. 1415–1428, Jul. 2015.
- [10] B. Komati, K. Rabenorosoa, C. Clevy, and P. Lutz, "Automated guiding task of a flexible micropart using a two-sensing-finger microgripper," *IEEE Trans. Autom. Sci. Eng.*, vol. 10, no. 3, pp. 515–524, Jul. 2013.
- [11] J. Y. Su *et al.*, "Design of tactile sensor array on electric gripper jaws for wire gripping recognition," in *Proc. IEEE Int. Conf. Autom. Sci. Eng. (CASE)*, Aug. 2014, pp. 1014–1019.
- [12] F. Chen, K. Sekiyama, P. Di, J. Huang, and T. Fukuda, "i-hand: An intelligent robotic hand for fast and accurate assembly in electronic manufacturing," in *Proc. IEEE Int. Conf. Robot. Autom.*, May 2012, pp. 1976–1981.
- [13] J. R. Amend, E. Brown, N. Rodenberg, H. M. Jaeger, and H. Lipson, "A positive pressure universal gripper based on the jamming of granular material," *IEEE Trans. Robot.*, vol. 28, no. 2, pp. 341–350, Apr. 2012.
- [14] R. Deimel and O. Brock, "A compliant hand based on a novel pneumatic actuator," in *Proc. IEEE Int. Conf. Robot. Autom. (ICRA)*, May 2013, pp. 2047–2053.
- [15] C. Blanes, M. Mellado, and P. Beltran, "Novel additive manufacturing pneumatic actuators and mechanisms for food handling grippers," *Actuators*, vol. 3, no. 3, pp. 205–225, Jul. 2014.
- [16] Y.-H. Chen and C.-C. Lan, "Design of a constant-force snap-fit mechanism for minimal mating uncertainty," *Mech. Mach. Theory*, vol. 55, pp. 34–50, Sep. 2012.
- [17] C.-C. Lan, S.-A. Yang, and Y.-S. Wu, "Design and experiment of a compact quasi-zero-stiffness isolator capable of a wide range of loads," *J. Sound Vibrat.*, vol. 333, no. 20, pp. 4843–4858, 2014.
- [18] Y. Liu, Y. Zhang, and Q. Xu, "Design and control of a novel compliant constant-force gripper based on buckled fixed-guided beams," *IEEE/ASME Trans. Mechatronics*, vol. 22, no. 1, pp. 476–486, Feb. 2016.
- [19] J.-Y. Wang and C.-C. Lan, "A constant-force compliant gripper for handling objects of various sizes," *ASME J. Mech. Des.*, vol. 136, no. 7, p. 071008, 2014.
- [20] C.-C. Lan and Y.-J. Cheng, "Distributed shape optimization of compliant mechanisms using intrinsic functions," *J. Mech. Des.*, vol. 130, no. 7, p. 072304, 2008.



Chih-Chieh Chen received the B.S. and M.S. degrees in mechanical engineering from National Cheng Kung University, Tainan, Taiwan, in 2014 and 2016, respectively.

His previous research interests were mechanism design, mechatronics, and robotics.



Chao-Chieh Lan (SM'14) received the B.S. degree in mechanical engineering from National Taiwan University, Taipei, Taiwan, in 2000, and the Ph.D. degree in mechanical engineering from the Georgia Institute of Technology, Atlanta, GA, USA, in 2006.

He is currently a Professor with the Department of Mechanical Engineering, National Cheng Kung University, Tainan, Taiwan. His research interests are in flexure-based mechatronics systems, robotics, multibody dynamics, and mechanism design.